optica

Integrated balanced homodyne photonic–electronic detector for beyond 20 GHz shot-noise-limited measurements

Cédric Bruynsteen,* Michael Vanhoecke, Johan Bauwelinck, and Xin Yin

Ghent University-imec, IDLab, Dep. INTEC, 9052 Ghent, Belgium
**Corresponding author: cedric.bruynsteen@ugent.be*

Received 29 January 2021; revised 13 July 2021; accepted 20 July 2021 (Doc. ID 420973); published 26 August 2021

Optical homodyne detection is used in numerous quantum and classical applications that demand high levels of sensitivity. However, performance is typically limited due to the use of bulk optics and discrete receiver electronics. To address these performance issues, in this work we present a co-integrated balanced homodyne detector consisting of a silicon photonics optical front end and a custom integrated transimpedance amplifier designed in a 100 nm GaAs pHEMT technology. The high level of co-design and integration provides enhanced levels of stability, bandwidth, and noise performance. The presented detector shows a linear operation up to 28 dB quantum shot noise clearance and a high degree of common-mode rejection, at the same time achieving a shot-noise-limited bandwidth of more than 20 GHz. The high performance of the developed devices provide enhanced operation to many sensitive quantum applications such as continuous variable quantum key distribution, quantum random number generation, or high-speed quantum tomography.

https://doi.org/10.1364/OPTICA.420973

1. INTRODUCTION

High-speed balanced homodyne detectors receivers have become essential building blocks in a multitude of applications dealing with sensitive measurements. In the quantum field, some common applications using balanced detection are: quantum random number generation (QRNG) [1–5], continuous variable quantum key distribution (CV-QKD) [6,7], characterization of quantum states [8–10], photonic quantum sensing [11,12], quantum computing [13–16] and coherent Ising machines [17]. The utility for balanced detection is not only limited to quantum applications, because it is also used in many other classical applications where sensitive optical measurements are critical, such as optical coherence tomography [18], coherent lidar [19], gas sensing [20], or (long-distance) coherent optical communications [21]. The fidelity, stability, and speed of these measurements are determined in large part by the balanced receiver. For instance, in CV-QKD, one of the largest contributors to the excess noise has been shown to originate from the electronic detector [22] or, in QRNG, the generation rate scales naturally with the noise and bandwidth performance of the detector [1–5].

A lot of progress has been made recently to increase the performance by monolithically integrating the optical front end [9,10,23,24]. The result of this progress is not only a reduction of the physical size of the devices, but it also allows for more interferometric stability, reduced insertion loss, and the use of high-bandwidth components that have been present in traditional telecom applications for many years. Silicon photonics has been expressed as a very suitable platform for the integration of quantum photonics because it is able to obtain high integration density, low losses, good passives [25], and high-speed photodetectors (PDs) with bandwidths up to 40 GHz [26]. All of these properties are beneficial to the design of balanced homodyne receivers.

Even though these integrated optical front ends make use of high-bandwidth components [10,23], the overall system speed is heavily constrained by the electrical bandwidth imposed by the readout electronics. The readout electronics in balanced homodyne detectors have typically been composed of discrete off-the-shelf packaged operational amplifiers and passives [10,27–30]. The packaging parasitics in these components impose an inherent limitation in noise performance and bandwidth. Only recently has a commercial integrated telecom amplifier been interfaced with integrated quantum photonics [9]. This resulted in a convincing increase in bandwidth while maintaining similar noise levels to discrete off-the-shelf approaches. Although using commercial telecom transimpedance amplifiers (TIAs) provides a convenient way to fully integrate the balanced receiver, the amplifiers are not designed with highly sensitive analog applications in mind. This typically results in suboptimal noise performance since it does not make sense for these amplifiers to operate at noise levels well below the shot noise limit, because having ultralow noise performance does not yield significant improvements toward the bit error rates in digital communications systems. However, in many applications such as CV-QKD, random number generation, or quantum tomography, it is imperative that the electronic noise is many times lower than the shot noise. By custom design, integrated TIA circuits with lower noise can be explored.

In this work, an optical front end is designed on imec's iSiPP50G silicon photonic platform [31]. The TIA, which converts the current produced by the optical front end, is designed in a 100 nm GaAs pseudomorphic high electron mobility transistor (pHEMT) technology. A framework is set out to map the different noise contributors and techniques are explored on how these contributors could be minimized.

2. DESIGN OF THE INTEGRATED DEVICES

A. Photonic Integrated Circuit

The schematic of the photonic integrated circuit (PIC) is shown in Fig. 1. Light is coupled into the chip via two grating couplers. In balanced homodyne detection, one grating coupler will receive the LO while the other receives the signal to be measured. In this implementation, one input contains a thermo-optical phase shifter, which is not used in this work, but could be used to implement CV-QKD with homodyne detection [22] or to perform phase scanning while measuring quantum states [9]. The two arms are optically mixed using a 2×2 multimode interferometer (MMI). Due to manufacturing tolerances, the power splitting ratio of the MMI can deviate slightly from the ideal 50:50 ratio. Likewise, the responsivity of the upper and lower photodiode can also exhibit some variation. These imperfections cause some common mode current to flow to the TIA. The rejection of this current is characterized by the common mode rejection ratio (CMRR). A poor CMRR is problematic for two separate reasons. First, because the TIA is DC coupled to the photodiodes, any DC current flowing into the TIA would cause a shift in the operating point of the transistors. To achieve low-noise performance, the TIA will require a large transimpedance gain, which means that a small amount of DC current can induce a large shift in the operating point. This results in a reduction of the dynamic range of the TIA. Second, a high CMRR cancels the classical noise such as the relative intensity noise (RIN) present in the LO [32]. This is crucial to maintain low-noise operation over the complete frequency range.

To improve the CMRR, two Mach–Zehnder modulators (MZMs) are added to the output arms of the MMI. The MZMs are biased in such a way that equal amounts of current are produced by each photodiode. This is monitored via two pins on the TIA that measure the differential DC input current. Alternatively, a Mach–Zehnder interferometer could also be used to improve CMRR [9,23]. Eventually the light reaches two lateral germanium photodiodes that exhibit very low junction capacitances (<10 fF). The photodiodes have a nominal responsivity of 1.1 A/W at a wavelength of 1550 nm and a 3 dB opto-electrical bandwidth in excess of 10 GHz. The currents produced by the photodiodes are subtracted via a common connection and the pads are connected to the TIA via bond wires.

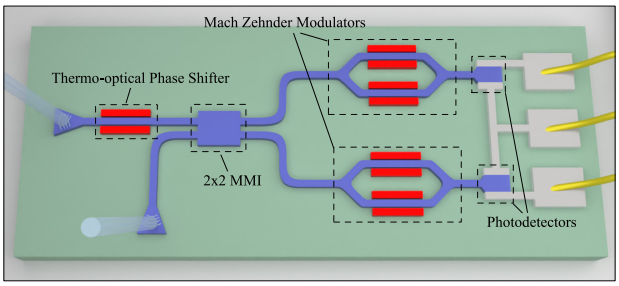

Fig. 1. Schematic of the photonic integrated circuit. Two grating couplers, a thermo-optical phase shifter, a 2×2 MMI, two Mach–Zehnder modulators and two photodiodes are depicted. The anode of the top photodiode and the cathode of the bottom photodiode are common such that the differential current flows to the subsequent TIA.

B. Transimpedance Amplifier

The low-noise transimpedance amplifier is designed to convert the weak differential current produced by the balanced photodetectors to a sufficiently strong voltage, which can be easily processed by an analog-to-digital converter (ADC), without distorting the signal or adding much noise. TIAs in earlier balanced detectors have usually been constructed by assembling discrete off-the-shelf components [27,33], or have used a commercial bare die TIA used in telecom applications [9]. The issue with discrete components is that the overall bandwidth of the system is limited by all the packaging parasitics that makes high speed (GHz+) operation at low noise not practically achievable. Commercial telecom TIAs are often designed with simple digital modulation schemes in mind (e.g., on–off keying) and single photodiode operation. This results in the TIA having poor linearity when either sinking or sourcing current, causing severe distortion for the analog applications that are targeted in this work. Linear commercial TIAs do exist, but are usually for high baud rate, long-reach coherent applications and would be too noisy for highly sensitive applications. In this work, a TIA with a bandwidth in excess of 1 GHz, linear operation, and ultralow noise performance is targeted.

A common figure-of-merit for balanced receivers is the quantum shot noise to classical noise ratio, measured with a vacuum input applied to the optical input port [9,10,22,34], commonly referred to as clearance. A large amount of clearance enables longer reach communications in CV-QKD and guarantees low overhead in QRNG, increasing the maximal random number generation rate. The clearance can be written as

$$\begin{aligned}\text{Clearance} &= 10\log_{10}\left(\frac{I_{n,\text{shot}}^2}{I_{n,\text{clas}}^2}\right)\text{[dB]}\\ &= 10\log_{10}\left(\frac{2q\overline{I_{\text{PD,bot}}}+2q\overline{I_{\text{PD,top}}}}{I_{n,\text{TIA}}^2}\right)\text{[dB]}.\end{aligned}\tag{1}$$

The shot noise density $I_{n,\text{shot}}^2$ is equal to $2q\overline{I_{\text{PD,bot}}}+2q\overline{I_{\text{PD,top}}}$, with $\overline{I_{\text{PD,bot}}}$ the average current flowing through the bottom photodetector and $\overline{I_{\text{PD,top}}}$ the average current flowing through the top photodetector. If the optical power is properly balanced, the average current flowing through the top and bottom photodetector is identical. The classical noise ($I_{n,\text{clas}}^2$) is mainly introduced by the TIA. To realize high levels of clearance it is essential that the TIA has a low input referred current noise density (IRND, $I_{n,\text{TIA}}^2$), which depends greatly on the topology of the TIA and the transistor technology. In this work, field-effect transistor (FET) type shunt-feedback TIAs are considered (Fig. 2), and the input referred current noise density is approximated by [35,36]

$$I_{n,\text{TIA}}^2 = \underbrace{\frac{4kT}{R_F}}_{\text{Contribution R}_F} \underbrace{+2qI_G+4kT\Gamma\frac{(2\pi C_{\text{in}})^2}{g_m}f^2}_{\text{Contribution Q}_1}+\ldots,\tag{2}$$

where $C_{\text{in}} = 2C_{\text{in}}^{\text{PD}} + C_{\text{in}}^{\text{TIA}}$ is the total input capacitance of the TIA, g_m is the transconductance of the input FET (Q_1), I_G is the gate current, Γ is Ogawa's excess noise factor [37,38], k is the

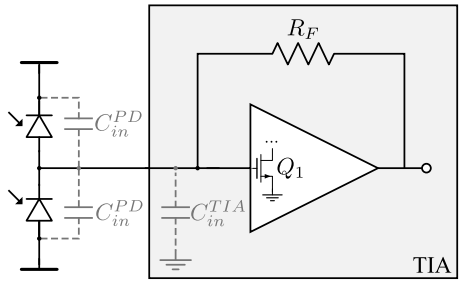

Fig. 2. Schematic overview of the TIA in combination with the balanced photodiodes. The two photodiodes are present on the PIC and each has an intrinsic capacitance $C_{\text{in}}^{\text{PD}}$. The TIA consists of a voltage amplifier with an input transistor Q_1 and a feedback resistor R_F. The voltage amplifier can consist of multiple gain stages. Each gain stage has a gain of A_0 and bandwidth of f_A, yielding a gain–bandwidth product of $A_0 f_A$.

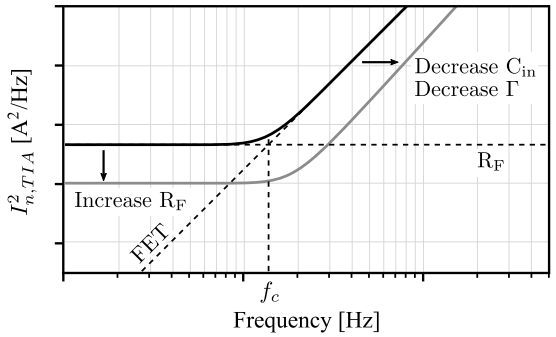

Fig. 3. Theoretical input referred noise density of the TIA $I_{n,\text{TIA}}^2$ as a function of frequency, see Eq. (2).

Boltzmann constant, and T is the absolute temperature. The noise contributed by the feedback resistor R_F has a white spectrum and is the dominant source of noise at low frequencies. At the corner frequency $f_c \approx \sqrt{g_m/(\Gamma R_F (2\pi C_{\text{in}})^2)}$, the transistor drain noise becomes the dominant noise source (Fig. 3). The $1/f$ noise is not taken into account because this should have a minimal effect, considering the frequency range of interest. Noise sources such as thermal noise generated by the substrate of the photodetectors or other secondary noise sources are not considered in this noise model. The clearance will be largest at low frequencies, and will drop rapidly above f_c. To have wideband low-noise performance, the goal is twofold: Maximize the feedback resistance (i.e., transimpedance) and increase the corner frequency at which the transistor noise becomes dominant.

The design of a TIA starts with the selection of an appropriate transistor technology. This selection will have a large impact on the achievable bandwidth, the maximum transimpedance, and the corner frequency f_c. For high-bandwidth applications it is important that the selected technology has a high transition frequency f_t, which allows for the transistors to still have gain at high frequencies. The maximal obtainable transimpedance gain R_T depends on the 3 dB bandwidth ($B W_{3\,\text{dB}}$), the gain-bandwidth product ($A_0 f_A$), the input capacitance (C_{in}), the phase margin of the TIA (ϕ_m), and the number of gain stages in the voltage amplifier (n), as given by the transimpedance limit [39]:

$$R_T \le \sqrt{2^{n+1}} \tan^n\left(\frac{90^\circ - \phi_m}{n}\right) \frac{(A_0 f_A)^n}{2\pi C_{\text{in}} B W_{3\,\text{dB}}^{n+1}}. \quad (3)$$

For a single-stage amplifier design the transimpedance limit simplifies to

$$\xrightarrow{n=1} R_T \le 2 \tan(90^\circ - \phi_m) \frac{A_0 f_A}{2\pi C_{\text{in}} B W_{3\,\text{dB}}^2}. \quad (4)$$

This equation implies that advanced technology nodes with a high f_t ($\sim A_0 f_A$) should allow for higher transimpedance values and hence improved low-noise performance at low frequencies. It also demonstrates the difficulty to manufacture high-bandwidth, low-noise TIAs. Considering single-stage amplifiers, if one would want to double the bandwidth for a given technology node ($A_0 f_0$ remains constant) and a given photodiode (C_{in} constant), one would need to reduce the feedback resistor by a factor of four. This causes the low-frequency noise to increase fourfold. For a three-stage amplifier, this becomes even worse, as the transimpedance would drop by a factor of 16. Even so, it doesn't mean that multistage amplifiers necessarily yield lower transimpedance values. It can be shown that multistage amplifiers can outperform single-stage amplifiers when the factor $A_0 f_A / B W_{3\,\text{dB}}$ is large [39]. This reaffirms the preference for a fast technology node with a high gain–bandwidth product.

Additionally, the corner frequency at which the noise of the input FET transistor becomes the dominant noise source, $f_c \approx \sqrt{g_m/(\Gamma R_F (2\pi C_{\text{in}})^2)}$, must be placed at a high frequency. This is achieved primarily by having a low input capacitance, which is comprised of a contribution by the photodiodes and by the TIA. Lateral waveguide photodiodes available in imec's iSiPP50G silicon photonics platform are used. These photodiodes have a very small junction capacitance (<10 fF). The capacitance contribution of the TIA can once again be reduced by selecting a fast technology node with a high f_t. Secondarily, the excess noise factor Γ can be lowered by selecting an appropriate technology. In this case, choosing a smaller technology node is considered to have adverse consequences, because short channel effects such as velocity saturation, carrier heating, vertical field mobility reduction, and channel length modulation impact Γ [40]. However, different FET technologies offer different noise factors. While silicon metal–oxide–semiconductor field-effect transistor (MOSFET) technologies exist in very small nodes with a high f_t, they have been shown to suffer from poor noise performance for small channel lengths [38,41,42]. High electron mobility transistors (HEMTs) are another type of FET that use III-V materials such as GaAs, GaN, or InP. Compared to silicon, these III-V materials achieve improved electron mobility and a higher saturation velocity, which yields high speed and low-noise devices [43]. For these reasons HEMTs have been used extensively in the design of low-noise amplifier monolithic microwave integrated circuits (MMICs) [44–46]. In this work, a 100 nm GaAs pseudomorphic HEMT (pHEMT) technology is used with a typical f_t of 130 GHz.

The transimpedance limit Eq. (3) also shows that amplifiers with a low phase margin ϕ_m are able to achieve higher transimpedance values or a higher bandwidth. However, low phase margin values also result in higher overshoot in the time domain response and reduced phase linearity. Considering the modulation schemes employed in telecom, these disadvantages can be tolerated as digital signals are being transmitted. Commercial amplifiers strive for a phase margin of 63° (i.e., a Butterworth response), which yields a good trade-off between bandwidth, ringing, and jitter [47]. This is not preferred as typical use cases for balanced homodyne receivers employ analog signaling. Therefore, a much

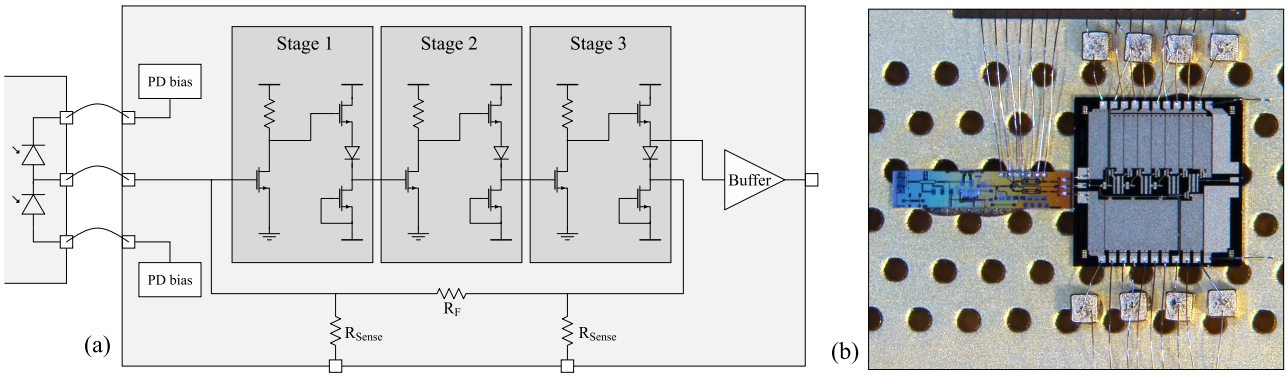

Fig. 4. (a) TIA schematic. The TIA consists of a three-stage amplifier and an output buffer. Two auxiliary pins are present to monitor the DC input current. (b) Micrograph of the manufactured devices, on the left side is the photonic IC and the on the right side is the TIA.

higher phase margin (>70°) is used in the design of the TIA, which eliminates ringing in the time-domain response.

For 100 nm pHEMT technology, it was found that a three-stage amplifier yields the highest transimpedance gain because the f_t is significantly higher than the targeted bandwidth. The schematic of the amplifier can be seen in Fig. 4(a). Each stage consists of a common source amplifier followed by a source follower with a level-shifting Schottky diode and current source. A 50 Ω buffer is added to isolate the TIA core from any outside loading and to provide 50 Ω matching toward measurement equipment. To measure the DC current flowing into the TIA, the voltage before and after the feedback resistor is monitored. The voltages are sensed via two large resistors (R_{sense}) so they do not significantly influence the high-frequency behavior of the circuit. The voltage difference between these nodes is equal to $I_{\text{in}}^{\text{DC}} R_F$. To obtain proper balancing, this voltage difference is used to tune the MZM on the PIC. Figure 4(b) shows the manufactured devices, with the PIC on the left and the TIA on the right. The output bonding pads of the PIC are placed close to the input bonding pads of the TIA. This allows for the use of short bondwires, preventing high frequency resonances. Wirebond capacitors, in addition to the on-chip decoupling capacitors, are placed close to the TIA to provide increased power supply decoupling. The TIA has a physical dimension of 2.4 × 2.4 mm and a power consumption of approximately 850 mW.

3. CHARACTERIZATION OF THE INTEGRATED CIRCUITS

This section discusses the performance of the balanced homodyne receiver using metrics such as the CMRR, a 3 dB bandwidth, output matching, and noise. At the end of this section, a comparison is made between this detector and the state-of-the-art in literature.

To characterize the CMRR, the PIC was connected to the TIA via wirebonds [Fig. 4(b)] and the output of the TIA was probed. A 1550 nm CW laser (Koheras Basiks E15 source, NKT Photonics), amplitude modulated with a sine wave, is supplied to one of the optical inputs. A polarization controller is added to optimize power coupling to the chip, minimizing polarization-dependent losses. For both the balanced and unbalanced measurements, the photodiodes were biased identically with a reverse bias of 1.5 V. For the unbalanced case, a slight imbalance was introduced by the on-chip MZMs. The optical power going into the chip was kept low as to avoid nonlinear distortion in the TIA. For the balanced case, the

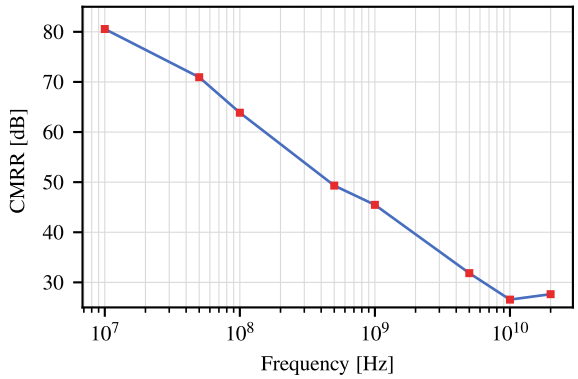

Fig. 5. Common mode rejection ratio with respect to frequency. A detailed discussion on how the CMRR is measured can be found in Supplement 1.

input current monitoring pins on the TIA were used to bias the MZM structures such that the voltage drop across the feedback resistor was zero. The resulting CMRR measured at several frequency points between 10 MHz and 20 GHz is shown in Fig. 5. At 10 MHz, the CMRR is 80 dB and decreases to 26 dB and 27 dB at 10 GHz and 20 GHz, respectively (Fig. 5). The degradation of the CMRR is attributed to differences between the individual photodiodes such as deviations in junction capacitance, contact resistance, substrate parasitics, and differences in the transit-time-limited bandwidth. This high level of CMRR is obtained partially thanks to the MZM structures but also due to the high levels of precision in matching the path lengths that are achieved in integrated photonics. Solutions using external variable optical attenuators and optical delay lines have reported a CMRR ranging between 29 dB at 1 GHz to 23 dB at 20 GHz [48]. A more in-depth explanation of how the CMRR was measured can be found in Supplement 1.

Next, the frequency response of the system was measured. To this end, a laser was modulated using a Fujitsu external 40 Gb/s $LiNbO_3$ MZM. The input ports of the MZM and the output of the TIA were connected to an Agilent N5247B PNA-X network analyzer. Using the on-chip MZM, a slight power imbalance is implemented. This is required so that the modulated signal raised above the noise floor and hence can be measured. The full two-port S-parameters are measured. The bandwidth of the external MZM was calibrated separately by connecting the modulated laser directly to a 70 GHz Finisar XPDV3120 photodetector and measuring the S-parameters of the MZM. The S_{21} transmission

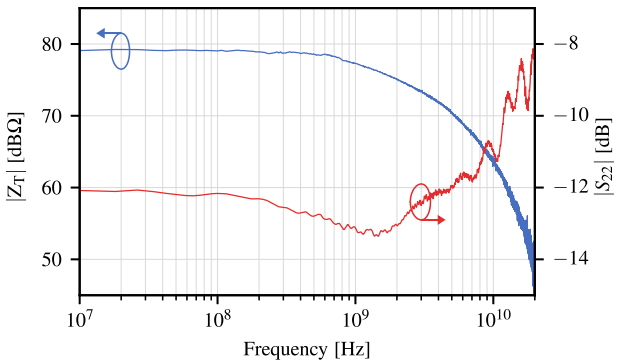

Fig. 6. Measured transimpedance gain and output matching parameter (S_{22}). Output is matched to 50 Ω if $|S_{22}|$ is less than −10 dB.

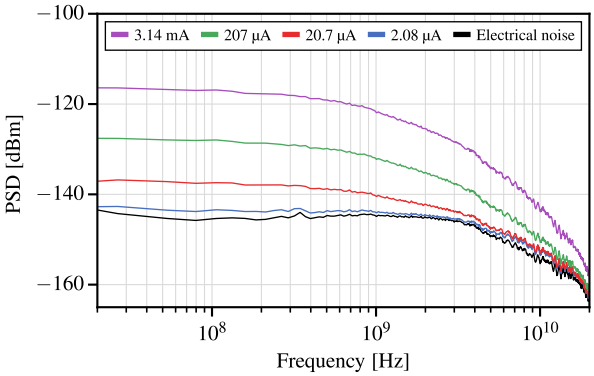

Fig. 7. Noise PSD at the output of the TIA for different photocurrents. Measurements are performed with an Agilent N9020A MXA signal analyzer.

coefficient of the calibrated S-parameters is used to measure the transimpedance gain, which can be seen in Fig. 6. A 3-dB bandwidth of 1.5 GHz is obtained. The output matching parameter S_{22} is also shown and is less than −10 dB below 10 GHz. This guarantees very little reflections in the frequency band of operation when connecting the TIA with other 50 Ω devices.

The noise performance of the balanced receiver is obtained by measuring the output noise power spectral density (PSD) with a vacuum input applied to one input grating coupler while the other grating coupler is supplied with the LO. To measure the PSD, an Agilent N9020A MXA signal analyzer is connected to the output of the TIA. Figure 7 shows the PSD for different photodetector currents. The photocurrents were measured using a Keithley 2400 source meter. A translation to optical power can be obtained by multiplying with the responsivity ($R = 1.1$ A/W). As expected, the noise power increases when the current increases. When plotting the PSD for a single frequency (f = 100 MHz) versus the current, Fig. 8(a) is obtained. For low currents (i.e., low levels of shot noise), the noise is dominated by the electrical background noise. This background noise is obtained separately by blocking both optical input ports. As the current increases the shot noise becomes the dominant source of noise. A maximum shot noise to electrical noise clearance of 28 dB is measured at 100 MHz for a current of 3.14 mA. We also observed a deviation of the ideal linear shot noise behavior at high optical powers. We believe this deviation could be caused by carrier recombination [49]. Figure 8(b) plots the normalized PSD, in which the PSD for photocurrents ranging between 207 μA and 3.14 mA are normalized with respect to the PSD at 65.3 μA of photocurrent and with the electronic noise removed. In an ideal linear detector, the normalized PSD should increase equally over the complete frequency range for increasing current; e.g., for the PSD corresponding to 207 μA of photocurrent, the increase is 10 log(207 μA/65.3 μA) = 5.01 dB. However, as was already clear from Fig. 8(a), at high optical power the detector saturates. This can be observed on the normalized PSD corresponding to 3.14 mA of photocurrent, where the normalized noise density dips below the expected value of 16.82 dB at higher frequencies. Taking a closer look at the clearance over the full frequency band [Fig. 8(c)], the clearance is high at low frequencies and decreases significantly at higher frequencies. Using Eq. (1), the IRND of the TIA can be calculated [solid red line in Fig. 8(c)]. When comparing the measured curve with the theoretical curve [dashed red line in Fig. 8(c)], a good correspondence between both can be observed. At low frequencies, the noise is dominated by the resistor while at high frequencies the noise is dominated by the input transistor drain noise. As the model in Eq. (1) is not all-encompassing, some deviation is expected, but the majority of the noise is characterized properly. The clearance was measured up to 20 GHz and remained shot noise limited. At 20 GHz, the shot noise is still twice as large as the electronic noise with a clearance of 4.8 dB.

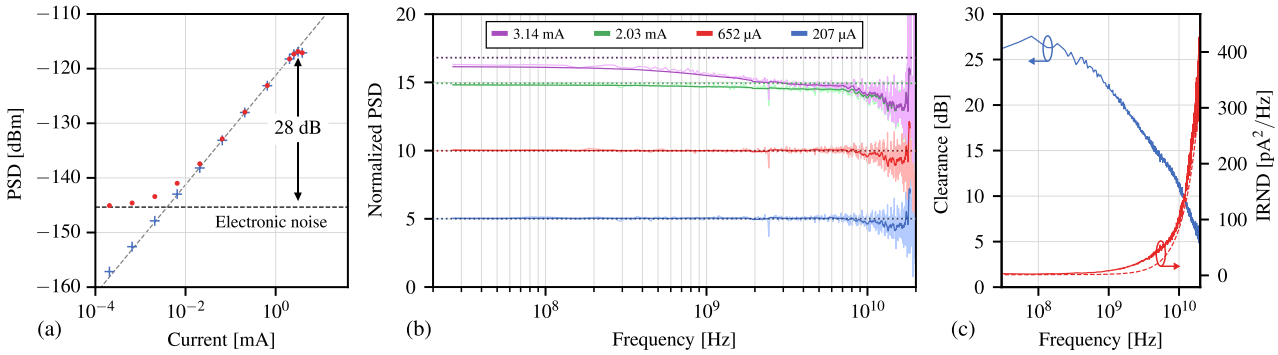

Fig. 8. (a) PSD measured at 100 MHz for different photocurrents flowing through the photodiodes. A maximum of 28 dB clearance between the electrical noise caused by the TIA and the shot noise is obtained at this frequency. (b) PSD for different photocurrents, normalized with respect to the PSD at 65.3 μA of photocurrent and with the electronic noise removed. The dark curves are moving averages of 20 points as the data becomes noisy at high frequencies. The dotted lines represent the expected values calculated using the ratio of the DC photocurrents. (c) Clearance curve with 2.03 mA photocurrent with respect to frequency. Because the noise of the TIA contains colored noise components, the clearance curve also reveals these components. The solid red curve is the IRND derived from the clearance using Eq. (1), and the dashed red line is the theoretical curve using Eq. (2).

Table 1. Comparison to State-of-the-Art Balanced Receivers

Reference	$BW_{3\,dB}$	BW_{shot}	Max Clearance	CMRR [Frequency]	
[9]	1.7 GHz	9 GHz	14 dB	52 dB [1 GHz]	[a, b]
[10]	150 MHz	300 MHz	11 dB	28 dB [50 MHz]	[a]
[27]	100 MHz	125 MHz	13 dB	46 dB [32 MHz]	–
[28]	40 MHz	–	14.5 dB	–	–
[29]	300 MHz	420 MHz	14 dB	54 dB [—]	–
[30]	2 MHz	–	37 dB	75 dB [2 MHz]	–
This work	1.5 GHz	20 GHz	28 dB	80–26 dB [0.01–20 GHz]	[a, b]

[a]The reference makes use of an integrated photonic IC.
[b]The reference makes use of an integrated TIA.

Table 1 shows how the balanced detector in this work compares to the state-of-the-art in literature. It is clear that detectors that use discrete TIAs [10,27–30] cannot reach bandwidths above 1 GHz. This is due to large parasitic capacitances that limit the obtainable bandwidth. The detector in [9] uses a commercial TIA in die form, so it is therefore able to reach much higher bandwidths and maintain noise levels comparable to the other references. The detector in this work is also able to achieve a high bandwidth while at the same time improving significantly in terms of noise. This is particularly clear in the shot-noise-limited frequency range (BW_{shot}). Only the work in [30] is able to reach comparably high levels of clearance, but requires a high optical power of 54 mW and is limited to 2 MHz bandwidth.

4. CONCLUSION

In this work a co-integrated balanced homodyne detector is reported. By designing a silicon photonics optical front end and a custom integrated TIA, a high bandwidth of 1.5 GHz and a reduction in noise with up to 28 dB clearance is achieved, which is significantly better compared to previous designs. A framework is used to model the noise generated by the TIA and provides useful insight in the trade-offs and optimization present in the TIA design. The high-bandwidth and low-noise performance translates to a large shot-noise-limited frequency range of 20 GHz. We believe that these integrated devices could provide significant enhancements to several noise-sensitive applications such as fast and long range CV-QKD systems, high-speed QRNG, optical coherence tomography, and accurate characterization of quantum states.

Funding. Horizon 2020 Framework Programme (820474); Fonds Wetenschappelijk Onderzoek (1SB1721N).

Disclosures. The authors declare no conflicts of interest.

Data availability. Data underlying the results presented in this paper are not publicly available at this time but may be obtained from the authors upon reasonable request.

Supplemental document. See Supplement 1 for supporting content.

REFERENCES

1. C. Gabriel, C. Wittmann, D. Sych, R. Dong, W. Mauerer, U. L. Andersen, C. Marquardt, and G. Leuchs, "A generator for unique quantum random numbers based on vacuum states," Nat. Photonics **4**, 711–715 (2010).
2. D. Drahi, N. Walk, M. J. Hoban, A. K. Fedorov, R. Shakhovoy, A. Feimov, Y. Kurochkin, W. S. Kolthammer, J. Nunn, J. Barrett, and I. A. Walmsley, "Certified quantum random numbers from untrusted light," Phys. Rev. X **10**, 041048 (2020).
3. M. Avesani, D. G. Marangon, G. Vallone, and P. Villoresi, "Source-device-independent heterodyne-based quantum random number generator at 17 Gbps," Nat. Commun. **9**, 1–7 (2018).
4. B. Xu, Z. Chen, Z. Li, J. Yang, Q. Su, W. Huang, Y. Zhang, and H. Guo, "High speed continuous variable source-independent quantum random number generation," Quantum Sci. Technol. **4**, 025013 (2019).
5. T. Gehring, C. Lupo, A. Kordts, D. Solar Nikolic, N. Jain, T. Rydberg, T. B. Pedersen, S. Pirandola, and U. L. Andersen, "Homodyne-based quantum random number generator at 2.9 Gbps secure against quantum side-information," Nat. Commun. **12**, 1–11 (2021).
6. F. Grosshans, G. Van Asschet, J. Wenger, R. Brouri, N. J. Cerf, and P. Grangier, "Quantum key distribution using Gaussian-modulated coherent states," Nature **421**, 238–241 (2003).
7. S. Pirandola, U. L. Andersen, L. Banchi, M. Berta, D. Bunandar, R. Colbeck, D. Englund, T. Gehring, C. Lupo, C. Ottaviani, J. L. Pereira, M. Razavi, J. Shamsul Shaari, M. Tomamichel, V. C. Usenko, G. Vallone, P. Villoresi, and P. Wallden, "Advances in quantum cryptography," Adv. Opt. Photon. **12**, 1012–1236 (2020).
8. G. Breitenbach, S. Schiller, and J. Mlynek, "Measurement of the quantum states of squeezed light," Nature **387**, 471–475 (1997).
9. J. F. Tasker, J. Frazer, G. Ferranti, E. J. Allen, L. F. Brunel, S. Tanzilli, V. D'Auria, and J. C. Matthews, "Silicon photonics interfaced with integrated electronics for 9 GHz measurement of squeezed light," Nat. Photonics **15**, 11–15 (2021).
10. F. Raffaelli, G. Ferranti, D. H. Mahler, P. Sibson, J. E. Kennard, A. Santamato, G. Sinclair, D. Bonneau, M. G. Thompson, and J. C. Matthews, "A homodyne detector integrated onto a photonic chip for measuring quantum states and generating random numbers," Quantum Sci. Technol. **3**, 025003 (2018).
11. B. J. Lawrie, P. D. Lett, A. M. Marino, and R. C. Pooser, "Quantum sensing with squeezed light," ACS Photon. **6**, 1307–1318 (2019).
12. S. Pirandola, B. R. Bardhan, T. Gehring, C. Weedbrook, and S. Lloyd, "Advances in photonic quantum sensing," Nat. Photonics **12**, 724–733 (2018).
13. N. C. Menicucci, P. Van Loock, M. Gu, C. Weedbrook, T. C. Ralph, and M. A. Nielsen, "Universal quantum computation with continuous-variable cluster states," Phys. Rev. Lett. **97**, 110501 (2006).
14. W. Asavanant, Y. Shiozawa, S. Yokoyama, B. Charoensombutamon, H. Emura, R. N. Alexander, S. Takeda, J.-I. Yoshikawa, N. C. Menicucci, H. Yonezawa, and A. Furusawa, "Generation of time-domain-multiplexed two-dimensional cluster state," Science **366**, 373–376 (2019).
15. M. V. Larsen, X. Guo, C. R. Breum, J. S. Neergaard-Nielsen, and U. L. Andersen, "Deterministic generation of a two-dimensional cluster state," Science **366**, 369–372 (2019).
16. J. E. Bourassa, R. N. Alexander, M. Vasmer, A. Patil, I. Tzitrin, T. Matsuura, D. Su, B. Q. Baragiola, S. Guha, G. Dauphinais, K. K. Sabapathy, N. C. Menicucci, and I. Dhand, "Blueprint for a scalable photonic fault-tolerant quantum computer," Quantum **5**, 392 (2021).
17. Y. Yamamoto, K. Aihara, T. Leleu, K. I. Kawarabayashi, S. Kako, M. Fejer, K. Inoue, and H. Takesue, "Coherent Ising machines–optical neural networks operating at the quantum limit," npj Quantum Inf. **3**, 49 (2017).
18. A. F. Fercher, W. Drexler, C. K. Hitzenberger, and T. Lasser, "Optical coherence tomography - Principles and applications," Rep. Prog. Phys. **66**, 239–303 (2003).
19. R. Wang, L. Chen, Y. Zhao, and G. Jin, "A high signal-to-noise ratio balanced detector system for 2 μm coherent wind lidar," Rev. Sci. Instrum. **91**, 073101 (2020).
20. J. Hodgkinson and R. P. Tatam, "Optical gas sensing: A review," Meas. Sci. Technol. **24**, 012004 (2013).
21. K. Kikuchi, "Fundamentals of coherent optical fiber communications," J. Lightwave Technol. **34**, 157–179 (2016).
22. F. Laudenbach, C. Pacher, C.-H. F. Fung, A. Poppe, M. Peev, B. Schrenk, M. Hentschel, P. Walther, and H. Hübel, "Continuous-variable quantum key distribution with Gaussian modulation—The theory of practical implementations," Tech. Rep. (2018).
23. G. Zhang, J. Y. Haw, H. Cai, F. Xu, S. M. Assad, J. F. Fitzsimons, X. Zhou, Y. Zhang, S. Yu, J. Wu, W. Ser, L. C. Kwek, and A. Q. Liu, "An integrated silicon photonic chip platform for continuous-variable quantum key distribution," Nat. Photonics **13**, 839–842 (2019).
24. C. Abellán, W. Amaya, M. Jofre, M. Curty, A. Acín, J. Capmany, V. Pruneri, and M. W. Mitchell, "Ultra-fast quantum randomness generation

by accelerated phase diffusion in a pulsed laser diode," Opt. Express **22**, 1645–1654 (2014).
25. J. W. Silverstone, D. Bonneau, J. L. O'Brien, and M. G. Thompson, "Silicon Quantum Photonics," IEEE J. Sel. Top. Quantum Electron. **22**, 390–402 (2016).
26. M. Pantouvaki, S. A. Srinivasan, Y. Ban, P. De Heyn, P. Verheyen, G. Lepage, H. Chen, J. De Coster, N. Golshani, S. Balakrishnan, P. Absil, and J. Van Campenhout, "Active components for 50 Gb/s NRZ-OOK optical interconnects in a silicon photonics platform," J. Lightwave Technol. **35**, 631–638 (2017).
27. Y. M. Chi, B. Qi, W. Zhu, L. Qian, H. K. Lo, S. H. Youn, A. I. Lvovsky, and L. Tian, "A balanced homodyne detector for high-rate Gaussian-modulated coherent-state quantum key distribution," New J. Phys. **13**, 13003 (2011).
28. S. Du, Z. Li, W. Liu, X. Wang, and Y. Li, "High-speed time-domain balanced homodyne detector for nanosecond optical field applications," J. Opt. Soc. Am. B **35**, 481–486 (2018).
29. D. Huang, J. Fang, C. Wang, P. Huang, and G. H. Zeng, "A 300-MHz bandwidth balanced homodyne detector for continuous variable quantum key distribution," Chin. Phys. Lett. **30**, 114209 (2013).
30. X. Jin, J. Su, Y. Zheng, C. Chen, W. Wang, and K. Peng, "Balanced homodyne detection with high common mode rejection ratio based on parameter compensation of two arbitrary photodiodes," Opt. Express **23**, 23859–23866 (2015).
31. A. Rahim, J. Goyvaerts, B. Szelag, J. M. Fedeli, P. Absil, T. Aalto, M. Harjanne, C. Littlejohns, G. Reed, G. Winzer, S. Lischke, L. Zimmermann, D. Knoll, D. Geuzebroek, A. Leinse, M. Geiselmann, M. Zervas, H. Jans, A. Stassen, C. Dominguez, P. Munoz, D. Domenech, A. L. Giesecke, M. C. Lemme, and R. Baets, "Open-access silicon photonics platforms in Europe," IEEE J. Sel. Top. Quantum Electron. **25**, 8200818 (2019).
32. H. Bachor and T. C. Ralph, *A Guide to Experiments in Quantum Optics* (Wiley, 2019).
33. Y. Wang, X. Chen, and L. Zhang, "High-speed balanced homodyne detector for quantum information applications," J. Phys. Conf. Ser. **844**, 12010 (2017).
34. F. Xu, B. Qi, X. Ma, H. Xu, H. Zheng, and H.-K. Lo, "Ultrafast quantum random number generation based on quantum phase fluctuations," Opt. Express **20**, 12366–12377 (2012).
35. E. Säckinger, *Analysis and Design of Transimpedance Amplifiers for Optical Receivers*, 1st ed. (Wiley, 2017).
36. T. C. Carusone, D. A. Johns, and K. W. Martin, *Analog Integrated Circuit Design*, 2nd ed. (Wiley, 2011).
37. K. Ogawa, "Noise caused by GaAs MESFETs in optical receivers," Bell Syst. Tech. J. **60**, 923–928 (1981).
38. E. Sackinger, "On the excess noise factor Γ of a FET driven by a capacitive source," IEEE Trans. Circuits Syst. I Regul. Pap. **58**, 2118–2126 (2011).
39. E. Sackinger, "The transimpedance limit," IEEE Trans. Circuits Syst. I Regul. Pap. **57**, 1848–1856 (2010).
40. D. Binkley, *Tradeoffs and Optimization in Analog CMOS Design* (Wiley, 2008).
41. C. H. Chen and M. J. Deen, "Channel noise modeling of deep submicron MOSFETs," IEEE Trans. Electron Devices **49**, 1484–1487 (2002).
42. A. Antonopoulos, M. Bucher, K. Papathanasiou, N. Mavredakis, N. Makris, R. K. Sharma, P. Sakalas, and M. Schroter, "CMOS small-signal and thermal noise modeling at high frequencies," IEEE Trans. Electron Devices **60**, 3726–3733 (2013).
43. S. Voinigescu, *High-Frequency Integrated Circuits* (Cambridge University, 2013).
44. L. Bogaert, L. Bogaert, H. Li, K. Van Gasse, J. Van Kerrebrouck, J. Bauwelinck, G. Roelkens, and G. Torfs, "36 Gb/s narrowband photoreceiver for mmWave analog radio-over-fiber," J. Lightwave Technol. **38**, 3289–3295 (2020).
45. G. Nikandish and A. Medi, "A 40-GHz bandwidth tapered distributed LNA," IEEE Trans. Circuits Syst. II, Exp. Briefs **65**, 1614–1618 (2018).
46. J. Hu and K. Ma, "A 1-40-GHz LNA MMIC using multiple bandwidth extension techniques," IEEE Microwave Wireless Compon. Lett. **29**, 336–338 (2019).
47. B. Razavi, *Design of Integrated Circuits for Optical Communications*, 1st ed. (McGraw-Hill, 2002).
48. K. Inagaki, T. Kawanishi, A. Kanno, and N. Yamamoto, "Direct measurement on frequency response of common mode rejection ratio in coherent receiver," in *42nd European Conference on Optical Communication (ECOC)* (2016), pp. 1–3.
49. I. A. Maione, G. Fiori, L. Guidi, G. Basso, M. Macucci, and B. Pellegrini, "Shot noise suppression in p-n junctions due to carrier recombination," AIP Conf. Proc. **1129**, 221–224 (2009).